Investigation of the influence of process parameters on dimensional accuracy and post-sintering crack formation in ceramic 3D printing for porcelain-based commercial resin

Investigation of the influence of process parameters on dimensional accuracy and post-sintering crack formation in ceramic 3D printing for porcelain-based commercial resins.

Alessandro Bove[1], Jean-Marc Tulliani[2], Manuela Galati[1], Flaviana Calignano*[,1];

[1]*Department of Management and Production Engineering (DIGEP) - Integrated Additive Manufacturing Center (IAM) - Politecnico di Torino, Corso Duca Degli Abruzzi, 24 - 10129 Torino, Italy*

[2]*Department of Applied Science and Technology (DISAT), INSTM R.U. Lince Laboratory - Politecnico di Torino, Corso Duca Degli Abruzzi, 24 - 10129 Torino, Italy*

*Corresponding author: flaviana.calignano@polito.it; Tel.: +39 011 090 7218

Abstract

Several commercial ceramic resins are nowadays available in the market of Additive Manufacturing, making more approachable ceramic stereolithography (CS) to an extended audience of users, from academic to industrial fields. Lack of knowledge in terms of material characterization and expected behavior in the manufacturing process are the main problems that involve difficulties in obtaining precise, dense, resistant, and crack-free ceramic parts. This article presents a characterization of a porcelain-based commercial ceramic resin for digital light processing (DLP), Porcelite® by Tethon 3D, and a study on the printing dimensional accuracy and cracks formation in sintered samples in dependence on the process parameters used have been performed. Two different Porcelite® resins with different solid loadings are available in the market. Rheological measurements, thermogravimetry combined with differential thermal analysis, field emission scanning electron microscopy observation, and X-ray diffraction allowed the complete characterization of the most loaded ceramic suspension. A design of experiment (DoE) approach led to planning the experimental work identifying the geometry of the samples, the process parameters, and their levels of variation to evaluate the aspects that influence dimensional accuracy when printing and crack formation during thermal treatment. The final volumetric shrinkage of components produced respectively with Porcelite® Bison (PB) and Porcelite® Universal (PU) is 19.3 ± 2.2 % and 41.1 ± 3.6 %. Solid loadings evaluated through TG-DTA are 52 wt.% for PU and 72 wt.% for PB. Statistical analyses highlight that layer thickness and degree of exposure influence accuracy in x- and y-directions, and for both resins, part thickness influences accuracy only in the x-direction for PB resin. Layer thickness, part thickness, and interaction are influential in the z-direction. The printed accuracy shows certain independence from the resin solid loading.

Keywords: ceramics, 3D Printing, digital light processing, sintering, debinding

1.Introduction

Additive manufacturing (AM) of ceramics covers nowadays an important role in biomedical, chemical, aerospace, and electronics industries for the ability to obtain objects with complex shapes and high levels of customization. Ceramics are quite versatile materials because of their good mechanical resistance combined with excellent thermal resistance and chemical stability and their biocompatibility for bone tissue regeneration [1, 2]. Different AM technologies are available for ceramic parts obtainments, such as vat photopolymerization (VP) [3, 4], fused filament fabrication (FFF) [5], binder jetting (BJ) [6, 7], and selective laser sintering (SLS) [8]. AM allows for reducing costs in terms of processing time and energy consumption concerning traditional technologies, including gel casting, tape casting, and injection molding [9]. Compared with FFF, BJ, and SLS 3D printing, VP processes, i.e. stereolithography (SLA) and DLP, enable the production of complex ceramic parts with maximum precision and optimum surface roughness [10–15]. A UV-light source in SLA and a digital micromirror device (DMD) in DLP technologies are employed to induce photopolymerization reactions in a layer-by-layer approach. In these processes, dimensional precision, mechanical characteristics, and reliability of geometrical features are affected by different aspects, such as the resolution of the light source, the rheological and optical characterization of the ceramic slurry, process parameters, and thermal post-processing [16]. The main goal in manufacturing 3D ceramic parts via VP processes is to obtain a high-density green ceramic, leading to higher mechanical properties after sintering. The development of highly loaded ceramic suspensions (typically 45–55% by volume) within a printable viscosity (within the range of 3,000-5,000 mPa·s [3]) is the key to achieving this goal. In the past decade, a few researchers focused on developing low-viscosity photosensitive ceramic suspensions loaded with various ceramic powders for DLP or SLA 3D printing technologies [17–21].

Although the concept of preparing the ceramic resin is similar to the SLA and DLP processes, there are also some differences due to the different photopolymerization sources: the rheology (viscosity and flow) of the ceramic resins must be modified and optimized for each process, the photo-initiator system is different for each case and requires in-depth studies to evaluate the effect of the different light absorbers to achieve the desired accuracy for each system. At the beginning of the development of ceramic resins for VP processes, the viscosity of the suspension had to be comparable to that of the pristine raw resin, i.e. less than 3,000 mPa·s, while the current VP printers are also able to work on suspensions with a viscosity of tens of Pa·s. However, this is often difficult because, on the one hand, a higher volume fraction of ceramic particles allows for less shrinkage and higher density (and therefore mechanical strength) after sintering. On the other hand, a lower ceramic load reduces viscosity to a minimum and avoids possible segregation of the solid content. Therefore, compromises need to be made. To overcome these difficulties and make ceramic additive manufacturing more industrially feasible, several commercial inks based on alumina, silica, and zirconia are already available on the market.

Truxova et al. [22] tested three industrial-manufactured ceramic resins: Ceramic Resin from Formlabs performed on the Form 2 SLA printer and Porcelite®, and Vitrolite® resins from Tethon 3D tested on a DLP printer. They found that crack formation cannot be avoided during thermal treatment, despite the changes in the geometry of the model, process parameters, and firing cycles. Porcelite® resin is a ceramic suspension characterized by porcelain clay dispersed in an acrylic monomer base which starts polymerization when excited by a light source at the wavelength of 405 nm. In a

study by Mei et al. [23], mechanical characterization of ceramic porous lattice structures was performed; Porcelite® was used as starting materials, and chemical vapor infiltration (CVI) was applied to samples to infill the internal porosities and microcracks formed during pyrolysis. Infiltration methods were also applied by Mummareddy et al. [24] to combine the strength of ceramic materials and the ductility of metals; in this research, Ceramic Resin by Formlabs was used for the sample production. Other studies [25, 26] analyzed lithography-based processes for producing dense ceramic parts, starting from commercial suspensions. Kovacev et al. [27] investigated the dimensional accuracy of ceramic lattice parts produced by DLP using a DoE approach for evaluating the influence of process parameters. Another work [28] conducted a measurement analysis on 3D printed ceramic parts which aims to define a model for the compensation of the dimensional error generated in the process.

This work aims to compare the processability of two different kinds of Porcelite® resins that are today available on the marketplace: PU, used by Truxova et al. [22] and dedicated to all types of 405 nm DLP systems according to manufacturer's indication, PB, a denser resin specifically thought for producer's 3D printing system.

The influence of process and post-process parameters on crack formation and dimensional accuracy were evaluated for both resins. First, the experimental process plane was set using the DoE approach. X-ray diffractometry (XRD) and field emission scanning electron microscopy (FESEM) analyses were conducted to evaluate the granulometry of the powder. Thermogravimetric analysis (TG) and differential thermal analysis (DTA) analyses validated the firing profile for the thermal post-treatment. Investigation on crack formation in fired samples, post-printing, and post-sintering dimensional evaluations were performed to compare printing accuracy and final volumetric shrinkage.

2. Material and Methods

2.1 DLP printer

Figure 1 reports a schematic representation of the DLP working process. The 3D Printer selected for this experimental work uses a bottom-up approach (Bison 1000, Tethon 3D, Omaha, Nebraska). Dimensions of building platform area are 110 mm (x-axis) x 60 mm (y-axis). The maximum building height is 138 mm. The light source is a UV LED projector with a 1980 x 1080 pixels resolution. The printing resolution in x/y directions declared on the printer datasheet is 57 µm.

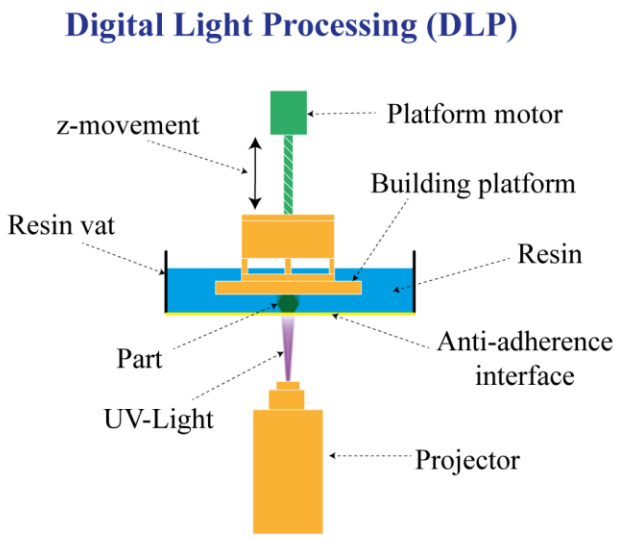

Figure 1. DLP System.

2.2 Resins characterization

TG-DTA (Setaram, Labsys Evo, Caluire, France) was used to determine the solid loading of the resins and to set up the thermal cycle of the debinding step. The measurements were performed on about 60 mg of the sample under static air with a 10 °C/min ramp from room temperature to 1100 °C. The viscosity of the resin was measured using a rheometer (Malvern, Kinexus Pro+, Malvern, UK) with a cup (C34) and bob (PC34) geometry, to allow the instrument to accurately control the temperature. The tests were conducted at 25 °C, 35 °C and 45 °C with a continuous increase of the shear rate from 0.1 up to 200 s^{-1} until the shear stress reached the limit of 3,000 Pa and the measurement stopped. The flow curve was recorded on the same sample after a 15 min rest for temperature stabilization and to enable relaxation of the system and was done twice. Finally, a certain amount of resin was dispersed into acetone on a magnetic stirrer to separate the powder from the polymeric resin. The dispersion was then filtered on a quartz paper filter (GVS Filter Technology, retention range 7-9 µm, Bologna, Italy) and thoroughly washed with acetone before drying in an oven at 40°C. Finally, the powder was gold sputtered before FESEM (Hitachi S4000, Tokyo, Japan) observations.

2.2.1 Resin viscosity

To determine the printing parameters that influence the processability of ceramic resin, different physical phenomena which take place during the process phases need to be understood. First, resin viscosity must be as low as possible to guarantee a correct vat recoating during building platform movement as suggested by Hinczewski et al. [3]. According to the Arrhenius equation, a temperature increase involves a reduction of the viscosity of ceramic suspensions. Vat heating has been set in the temperature range of 40 – 45 °C for PB, and 30 – 35 °C for PU, since preliminary tests confirmed the reduction of the viscosity of resins due to temperature increase. Also, the separation force generated

during platform elevation needs to be reduced to avoid damage to the part or FEP separation film [29], so the speed of the platform motor was reduced to 1 mm/s.

2.2.2 Optical parameters

Ceramic suspensions are obtained by mixing powders into acrylate-methacrylate monomers [30]. Light intensity (LI) and exposure time (ET) influence the degree of energy dose per area (*E)*, and they are the most important parameters in terms of curing behavior [31], according to Jacob's equation (1).

$$C_d = D_p \, ln\left(\frac{E}{E_c}\right) \tag{1}$$

Where C_d, D_p, and E_c are the cure depth, the depth of penetration of light, and the critical energy corresponding to which the gel point is reached, respectively. Preliminary tests showed that a more restricted variation field for LI could be considered for evaluation of printing accuracy since overcuring effects occurred aggressively for the tested resins. For this reason, only ET was considered for energy density regulation in this experimental study, as shown in the DoE in Table 1. Scattering phenomena in ceramic suspension cause broadening effects, resin sensitivity in horizontal direction, and reflections of incident light bring to accuracy losses [32]. LI values were fixed at 2.2 mW/cm^2 for PB and 3.9 mW/cm^2 for PU, as suggested by the manufacturer's indications. The difference between the values chosen for the two resins is due to the different solid loading. Cure depth needs to be lower for resin with higher solid loading to reduce the effect of scattered light [33].

2.2.3 Geometry of samples and thermal treatments

Different tests have been performed to evaluate the influence of geometry and building orientation of samples in post-sintering crack formation. Initially, cubic samples with side lengths of 7 mm, 10 mm, and 15 mm were produced (Figure 2a). Figure 2b reports the cracks generated on cubic samples of PU. The firing cycle followed for each resin corresponds to the one indicated in the producer's guide (Figure 3). The thermal treatment includes two different steps with different aims. The low-temperature treatment (debinding) is the most critical for crack generation, while the high-temperature step allows to sinter of parts and then enhances their mechanical properties. The variations to the debinding cycle were applied to the thermal treatments suggested in the resin manufacturer's guides (Figure 3) to reduce the effect of internal pressures in the most critical temperature range highlighted in TG-DTA curves.

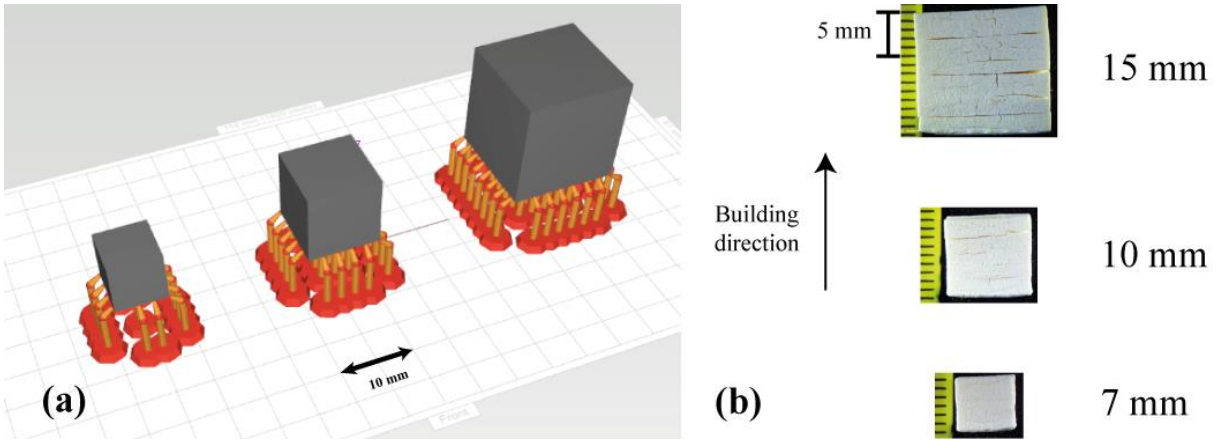

Figure 2. (a) Sample's orientation on the build platform; (b) post-sintering cracks.

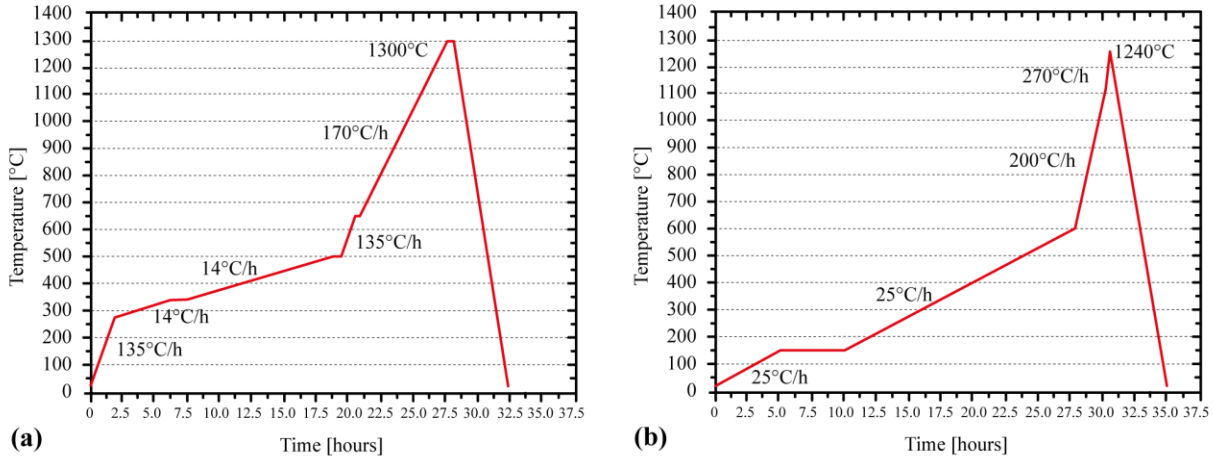

Figure 3. Thermal treatments proposed in resin's producer's guide; (a) PB firing cycle, (b) PU firing cycle.

The dimension of 10 mm for the side of the cube of the preliminary tests has been evaluated to be a good compromise between both dimensional accuracy study and thermal cycle evaluation, so a second attempt was made by designing thin walls with an area of 10 x 10 mm^2 and different widths. Thin walls (Figure 4) were oriented with the height parallel to the z-direction and produced with both resins. The geometry consisted of thin walls hollowed with 8 regular hexagons. The samples were produced also varying the side of the hole (0.1, 0.5, 1 mm) were also included to evaluate if the presence of holes in the body could help gas evacuation during debinding.

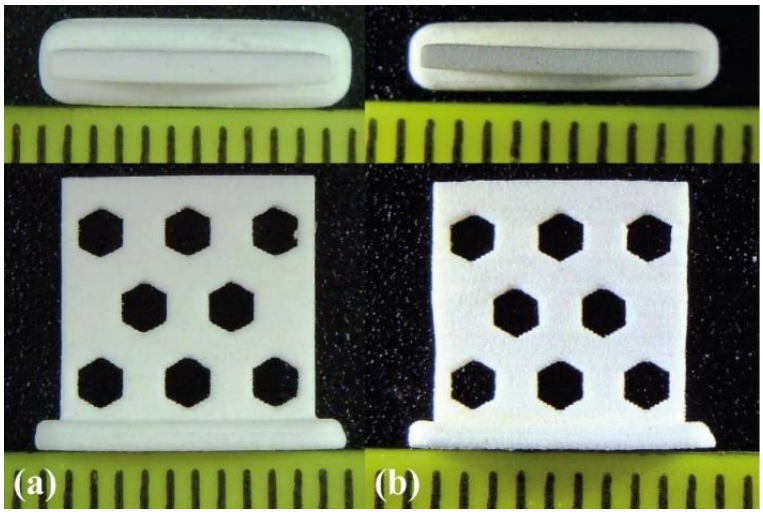

Figure 4. Sintered thin walls with honeycomb structure (1 mm of hexagon side): (a) PB top and side view, (b) PU top and side view.

In these tests, the thermal cycle was unchanged for PB, while for PU, the debinding stage was slowed down significantly (Figure 5). However, the problem of cracking was not solved.

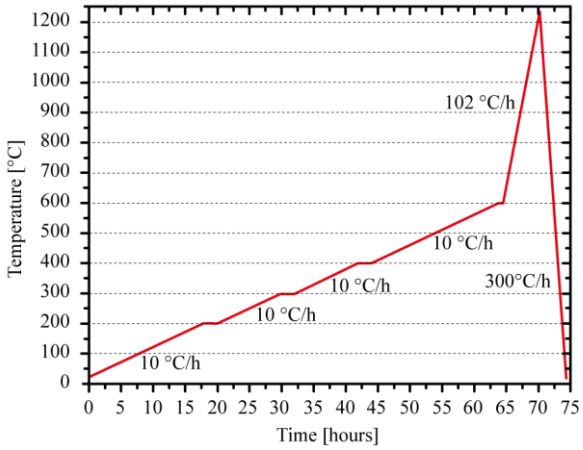

Figure 5. The new thermal cycle was determined based on the TG-DTA curve of PU resin (Figure 12).

The evidence that emerged from these preliminary tests is that crack formation occurs when part thickness increases and that the extension of the inter-layer area, depending on building orientation, favors gas evacuation. Honeycomb holes generated do not help the debinding; instead, they introduce instability points corresponding to which micro-cracks can start propagation, especially for resins with low solid loadings. Finally, bulk walls with different thicknesses (0.5, 1, 2, 3, 4, 5 mm) positioned with the major area normal parallel to the z-direction were chosen as investigating samples (Figure 6**Errore. L'origine riferimento non è stata trovata.**). The base plate was eliminated to avoid

possible warping and differences in shrinkage between the sample and the plate that can increase internal stresses during post-treatment.

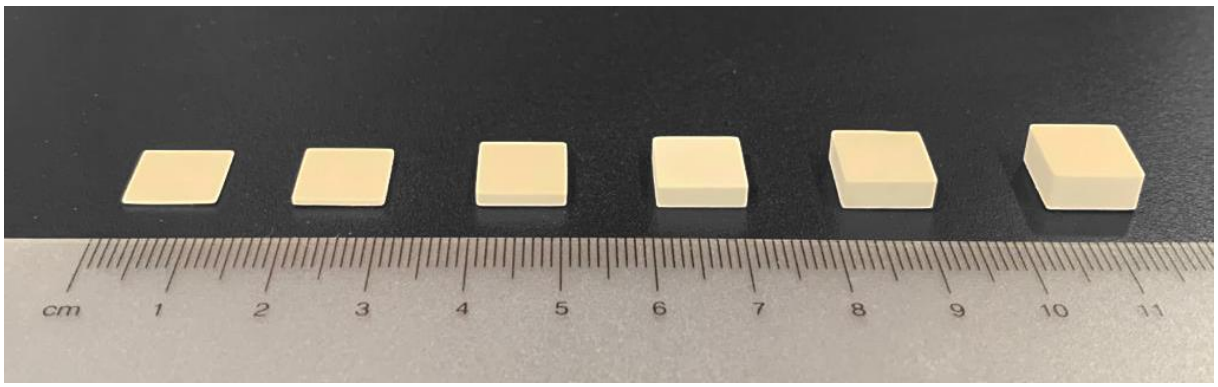

Figure 6. Samples with final geometry selected.

2.3 3D printing process

A DoE approach was used to select the process parameters window. In the first step, the limits of the parameters involved in the printing process were identified (Figure 7). For the layer thickness (LT) parameter, a value of 50 µm was selected as the lower limit, as the value of 25 µm induced errors during production, probably due to the increase in the number of separation steps between two successive cured layers. Furthermore, this lower value led to longer printing times. To evaluate the occurrence of cracking, samples were produced with 6 levels of part thickness (PT), from 0.5 mm to 5 mm. ET depends on the optical behavior of the resin. The parameter Degree of Exposure (DE) was introduced for a deeper comparison between resins. DE is a multiplication factor for LT, so ET is calculated as a function of LT. Limits of DE were found, excluding higher values for the predominant scattering effect occurring and lower values for job failure due to uncorrected adhesion between layers. Three levels of DE were selected. A full factorial approach was selected for the DoE (Table 1), so 36 samples were produced for each resin. For printability of samples, upper and lower limits of LT and DE needed to be established (Figure 7). The higher DE value was excluded because, despite the printability of the samples, the scattering effects were greater in the preliminary tests for such a long exposure, affecting the dimensional accuracy.

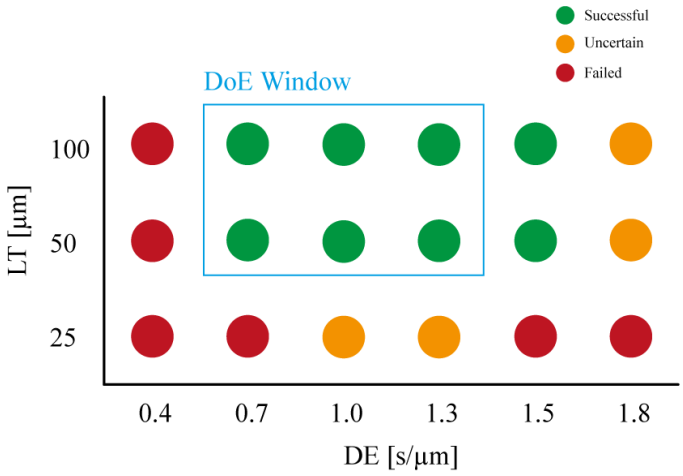

Figure 7. The window of parameters. Uncertain results refer to that experiment cases which are characterized by non-repeatability or other issues affecting printability.

After printing, supporting structures were removed, and uncured resin was washed through immersion an isopropyl alcohol (IPA) bath.

Observations of samples were made through a stereomicroscope Leica S9i.

Table 1. Design of Experiment for sample production

Factors	Abbreviation	Levels
Layer Thickness [µm]	LT	50, 100
Degree of Exposure [s/µm]	DE	0.7, 1.0, 1.3
Part Thickness [mm]	PT	0.5, 1, 2, 3, 4, 5

2.4 Debinding and Sintering

After printing two last treatments, debinding and sintering, are required to remove the polymeric binder and to achieve a good level of density of the parts and mechanical properties. The thermal cycles depicted in Figure 3 (recommended by the manufacturer) were followed to treat the printed parts. Both treatments were conducted in an air atmosphere, in the furnace (Nabertherm LHT, Lilienthal, Germany). The temperature of 1300 °C was reached during the sintering treatment for PB samples and kept for 30 minutes, and 1240 °C for PU samples without holding time.

2.5 Sample characterization

2.5.1 Measurements

Green parts and sintered sample sizes were measured with a digital caliper (with a resolution of 0.01 mm). Measured values of length, width, and height of green samples were compared with the respective nominal sizes to determine the specific directional accuracy, according to Eq. (2). A_i is the accuracy in the i direction (x, y, or z), i_0 represents the nominal size and i_m is the measured length. Absolute value was introduced to standardize accuracy for dimensions

smaller and larger than the nominal value. Volumetric shrinkage was calculated according to Eq. (3), where *S* is the volumetric shrinkage, V_{ps} is the post-sintering measured volume, V_m is the measured volume of green samples.

$$A_i = 1 - \left|1 - \frac{i_0}{i_m}\right| \tag{2}$$

$$S = \left(1 - \left(\frac{V_{ps}}{V_m}\right)\right) \% \tag{3}$$

The geometrical density of the samples was determined by weighing the sintered samples on a precision balance (Sartorius Extend, Goettingen, Germany; precision of 0.1 mg) and dividing their weight by the respective volumes calculated from previous geometrical measurements.

2.5.2 XRD

XRD patterns were collected on the printed and the sintered samples on a Pan'Analytical X'Pert Pro apparatus in the 2θ range 5-70° with a step size of 0.003° and a time per step of 21.42 s. The fired samples were manually ground in an agate mortar with an agate pestle before analysis.

3. Results and discussion

3.1 FESEM observations of the powder

The observation of the ceramic powder after resin removal (PB sample) revealed a rather fine ceramic raw material (Figure 8). The fine ceramic particles allowed us to fix the gap between the disc tool and its plate to 0.5 mm during viscosity measurements (in the § 3.2 Viscosity measurements). The agglomerates are probably due to some residual polymeric resin not being completely removed during acetone washing.

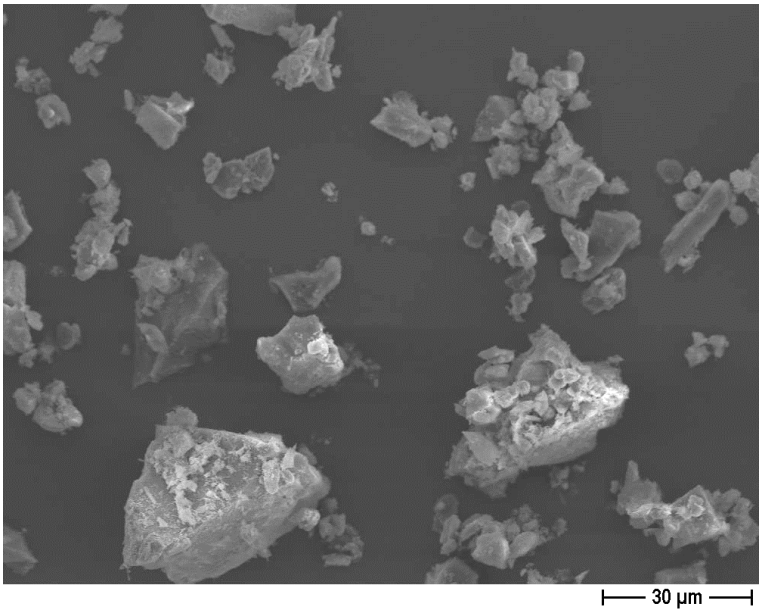

Figure 8. FESEM micrograph of the dried ceramic powder after acetone washing (PB sample).

3.2 Viscosity measurements

In this study, the rheological behavior (flow curve) of the PB resin could be well described by a second-order polynomial in the shear rate range from 0.1 to 200 s^{-1} (Figure 9a, Table 2). On the contrary, a linear fit, even if with a good coefficient of correlation (R^2 close to 1), led to a negative intercept on the abscissa axis, which has no sense [34]. A slight transition to shear-thickening behavior starts at high values of shear rate, specifically at 45 °C (Figure 9b). The polynomial model can be written according to Eq. (4):

$$\tau = c_1 + c_2 \cdot D + c_3 \cdot D^2 \tag{4}$$

where c_1 is the yield point in Pa and c_2 and c_3 are the first and second-order coefficients respectively, and D is the shear rate. In the current case study, the viscosity decreased with the temperature as shown in Figure 9b, as expected. At 45 °C, the measured viscosity was slightly high for stereolithography, where values below 5 Pa·s are targeted to ensure satisfactory layer recoating [3]: in the shear rate range from 1.42 s^{-1} to 193.6 s^{-1}, the average viscosity value was equal to 8.94 ± 0.49 Pa·s. The relatively constant viscosity as a function of the shear rate (only at 45 °C) is also depicted in Figure 9b.

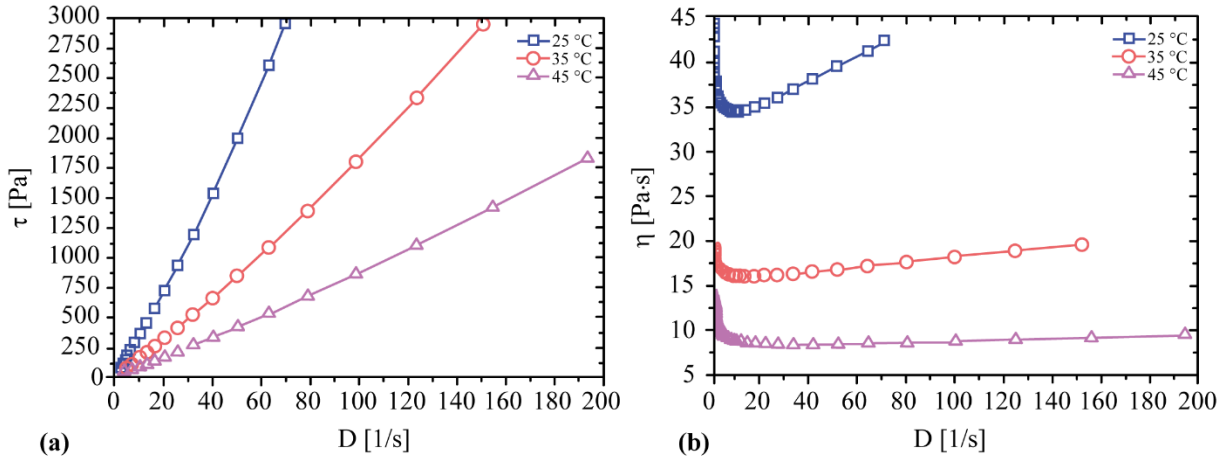

Figure 9. Flow curves of the PB resin at different temperatures: shear stress vs shear rate (a); viscosity vs shear rate (b).

Table 2. Results of the polynomial fit of the flow curve

Measurement temperature (°C)	Yield point (Pa)	C_2	C_3	R^2
25	4.52	32.38	0.14	1
35	2.18	15.43	0.03	1
45	3.32	8	0.01	1

3.3 XRD

XRD patterns of the printed resins (Figure 10) revealed the peaks of quartz (SiO_2, JCPDF card n° 46-1045) as the main phase, while alumina (Al_2O_3, JCPDF card n°10-0173) and kaolinite ($Al_2O_3.2SiO_2.2H_2O$, JCPDF card n° 14-0164) are secondary phases.

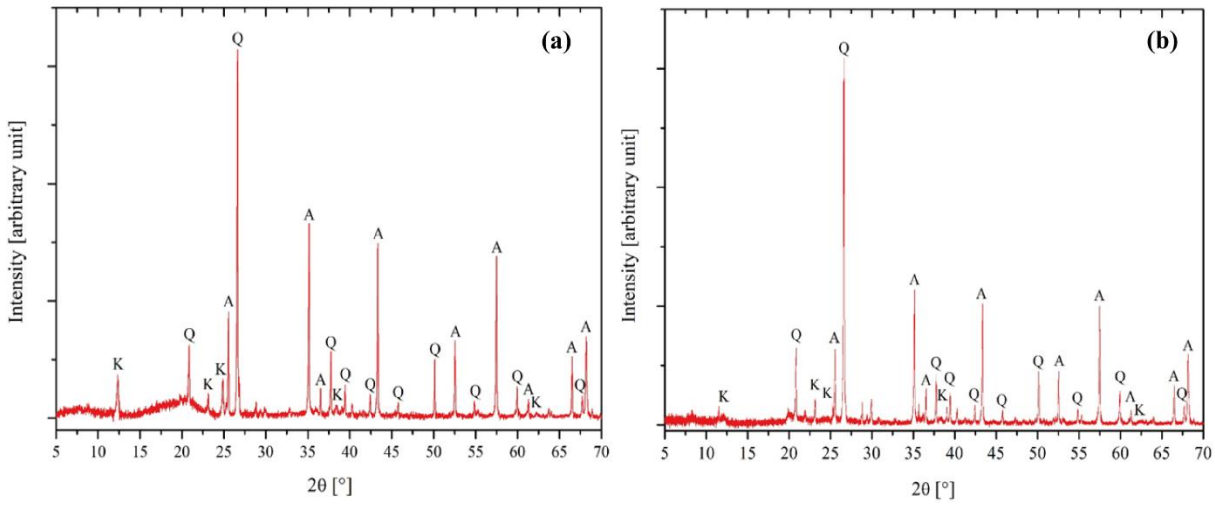

Figure 10. XRD pattern of the as-printed resin: PU (a); PB (b). (K=kaolin, Q=quartz, A=alumina).

The sintered samples (Figure 11) evidenced the peaks of alumina (JCPDF card n°10-0173) and mullite ($3Al_2O_3.2SiO_2$, JCPDF card n° 15-0776) as the main phases. Cristobalite (SiO_2, JCPDF card n° 39-1425) was found as a secondary phase. A broad hump ranging from 20 to 30°, with a maximum of about 22-23° is probably due to amorphous silica. Other peaks at 26.6°, 27.5°, 28.9° and 35.4° in 2θ were not identified. These results are expected, being the resins alumina silica resins, as declared by the manufacturer.

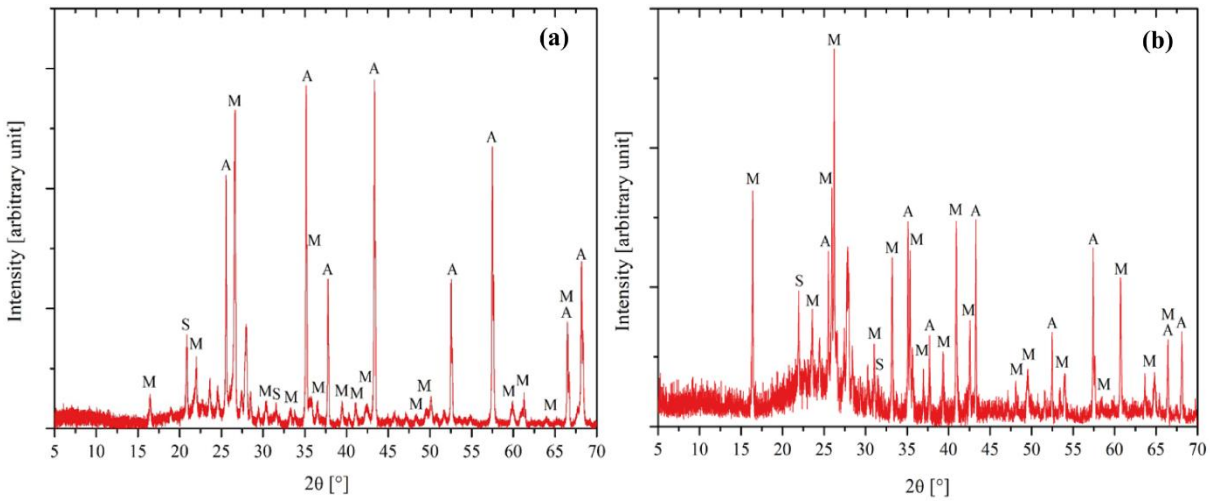

Figure 11. XRD patterns of the sintered sample: PU (a); PB (b). (M=mullite, A=alumina, S=silica).

In a mixture of 38.2 wt.% of calcined kaolin (metakaolin), 3.5 wt.% of silica, and 27.8 wt.% of alumina, during the thermal treatment, the mullite phase is formed at about 1100 °C [35]. XRD pattern (not shown here) of the PU resin fired at 1100 °C confirmed these results: only the peaks of quartz (JCPDF card n°46-1045), corundum (Al_2O_3, JCPDF card n°46-1212), cristobalite (SiO_2, JCPDF card n°39-1425) and probably of calcium aluminum silicate ($Al_{1.77}Ca_{0.88}O_8Si_{2.23}$, JCPDF card n°52-2344) were evidenced. The presence of calcium could be due to some calcium oxide/calcium carbonate addition as a sintering aid. These results are also in agreement with TG-DTA measurements (Figure 12) where no crystallization peak was detected below 1100 °C.

The raw materials and the sintered materials composition seem to be close to that of high alumina refractories [36], specifically HA75 formulation, according to the standard EN ISO 10081-1:2005 (Classification of dense shaped refractory products, Part 1: Alumina-silica).

3.4 TG-DTA measurements

The TG-DTA curve of the printed PU resin (Figure 12a) mainly evidenced four endothermic peaks at 226.4, 393.9, 448.9, and 509.9 °C due to the resin decomposition steps. The derivative curve (not shown here) indicated that the maximum decomposition rate was about 440 °C. The thermal decomposition is almost completed at 620 °C (mass loss of about 48%), while the final mass loss was 49.3% at 1100 °C. Thus, the solid loading was estimated to be equal to 51.7 wt.%. The PB resin TG-DTA curve (Figure 12b) evidenced five endothermic peaks at 429.2, 441.7, 455.9, 469.6, and 517.2 °C. However, the derivative curve also showed a maximum decomposition rate at about 440 °C. The thermal decomposition is again almost finished at 620 °C (mass loss of about 26.5%) with a final mass loss of 28.5% at 1100 °C. In this case, the solid loading was equal to 71.5%. Except for the peak at 226.4 °C, maybe due to the evaporation of some solvent, the two polymeric resins are probably not so different from each other but, in any case, the solid loading is much higher in the PB resin.

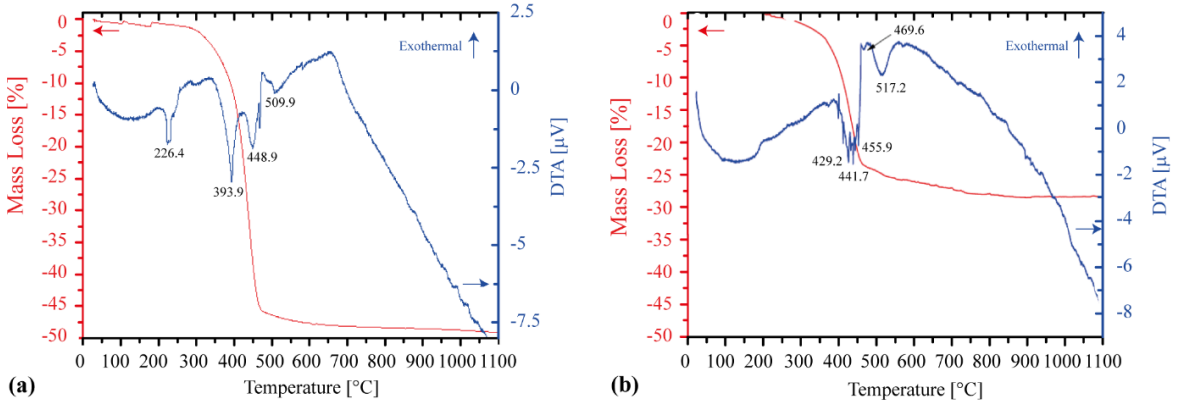

Figure 12. TG-DTA curve of the resin: PU (a); PB (b).

3.5 Thermal treatment and cracks generated

Different behaviors between the two resins have been found. The outcomes of successful/failed samples are displayed in Figure 13. Delamination phenomena occur when crack propagation occurs between two adjacent layers, without propagation in the z-direction. Intra-laminar cracks have been highlighted especially in PU samples, where vertical propagation of cracks was favored. A comparison between delamination and intra-laminar cracks in PB samples and PU samples is displayed in Figure 14. The type of crack found in PU samples is similar to that found by Truxova et al. [22]. Instead, random cracks were generated from a single defect or microporosity and propagated in all directions. This type of cracks can be visualized on the top surface of samples (Figure 15). Random cracks were not frequent in PB samples, and they were highlighted starting from higher values of part thickness; in PU samples, both types of cracks were found for all values of part thickness.

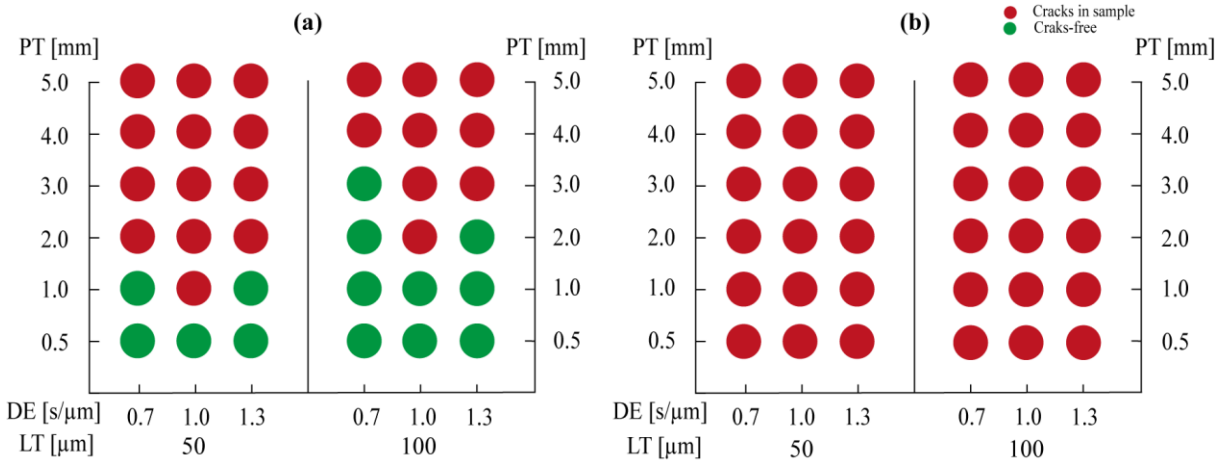

Figure 13. Outcomes of experiment on cracks formation for (a) PB, (b) PU.

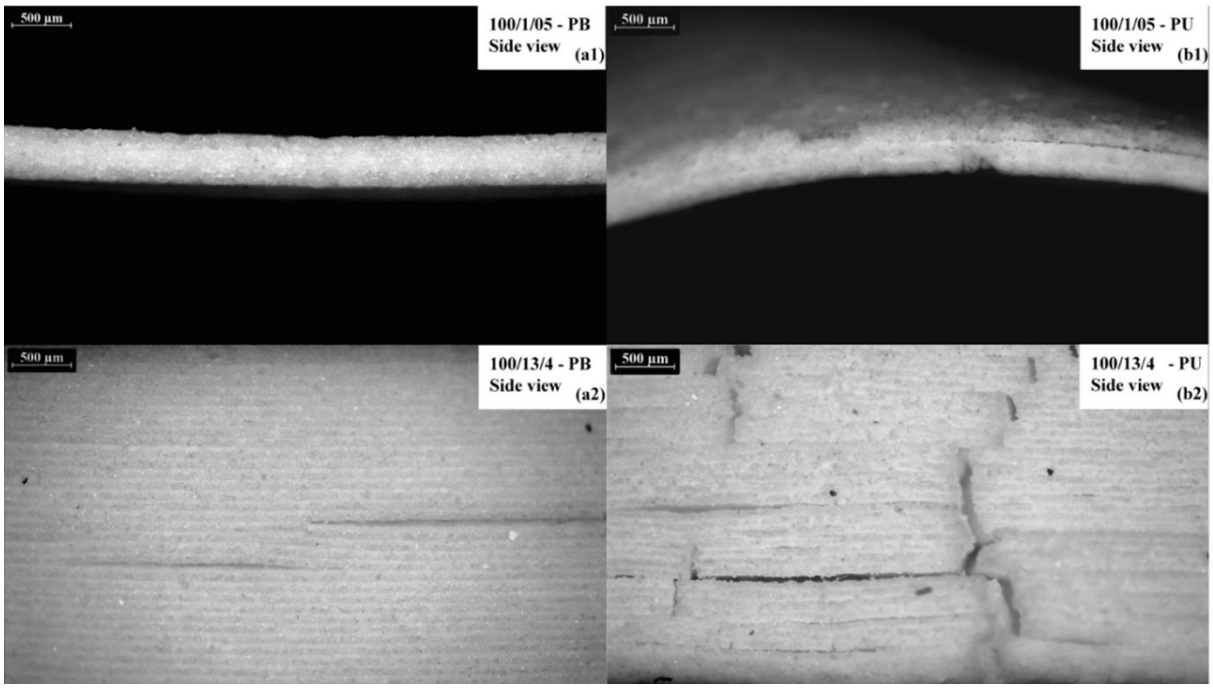

Figure 14. Stereomicroscope images; (a1) side view of a PB sample 0.5 mm thick and crack-free; (a2) side view of a PB sample 4 mm thick with delamination effects; (b1) side view of a PU sample 0.5 mm thick with high warping and delamination effects; (b2) side view.

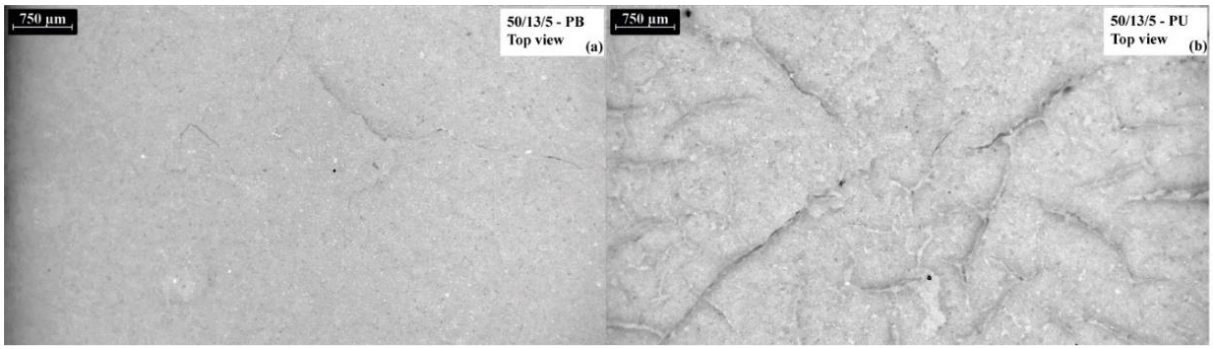

Figure 15. Stereomicroscope images. Cracks in PB (a) and PU (b) samples (Top views).

Differences in proportion between organic binder and ceramic powders result in a raise in the micro-channels formation in the first stage of the debinding process. In a study by Wang et al. [37] the two different stages of debinding process, low and high temperatures, were studied. In the low-temperature stage, micro-channel generation is due to the melting and gasification of the first organic compounds. In the high temperatures stage, oxidation of carbon compounds occurs quickly, resulting in a release of a large amount of heat, which is difficult to control in an air environment. Types of cracks generated depend not only on solid loading but also on resin composition. In low solid

loading resins, adding a non-reactive compound can result in a more distributed weight loss in the debinding temperature range, reducing the pressure peaks generated in heating [38].

3.6 Post-printing accuracy

3.6.1 Accuracy in x/y directions

Post-printing accuracy in x/y directions is influenced by optical phenomena involved during photopolymerization and projector resolution. Printing precision was calculated according to Eq. (2), and results are reported in Figure 16. All lengths measured are larger than the nominal size. This highlights that probable shrinkage due to photopolymerization reaction could be overshadowed by scattering phenomena in the two resins [39], so only a surplus in sizes on the x/y plane is revealed. Results show that printing accuracy is not the same in the x and y directions. There is no reason to consider differences in scattering phenomena along the two axes. Consequently, the x/y accuracy of the projector cannot be considered equal. The mean values for PB accuracy achieved in the x and y directions are 96.50 ± 0.48 % and 98.21 ±0.42 %, respectively, while for PU samples, are 97.05 ± 0.87 % and 98.37 ± 0.9 %.

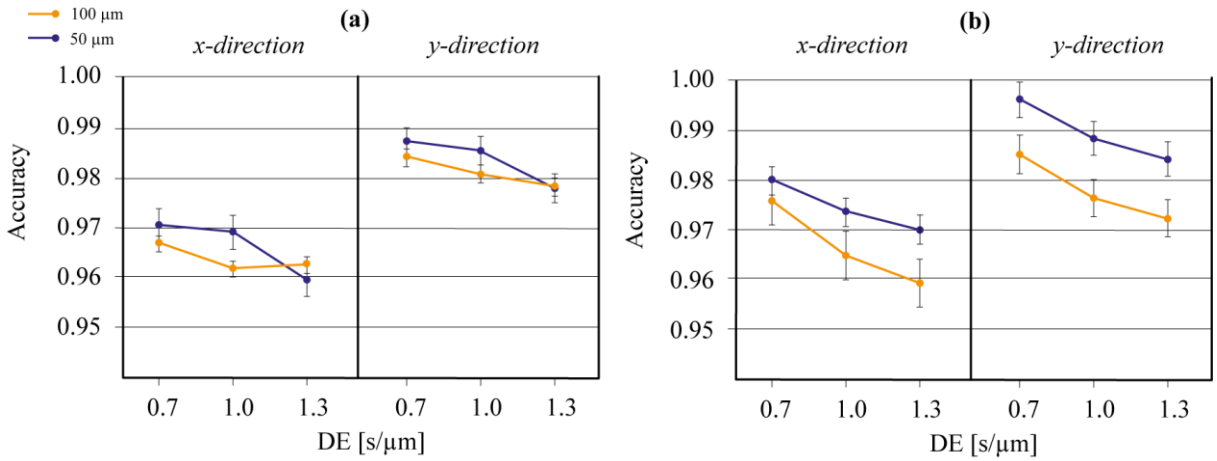

Figure 16. PB (a) and PU (b) accuracies in the x-direction and y-direction.

Deviation from the nominal size in x/y directions becomes more evident in samples processed with higher DE. Significant correlation coefficients (p-value < 0.05) are presented in Table 3 and confirm that DE and LT influence printing precision in both directions and for both resins with a 95% of confidence, while part thickness has influence only in the x-direction for PB samples. In PU samples, part thickness and all interactions between parameters affecting the accuracy can be excluded almost in all cases (Table 4). Considerations on DE and its increasing influence on printing accuracy in dependence on resin solid loading are by prediction done on scattering effect. In the x direction, the test gives evidence of a different impact of part thickness on the analysis; only in the x-direction, it seems to be influential for PB resin.

Table 3. ANOVA for evaluation of the influence of DE, LT, PT on x and y accuracy for PB. DF= degree of freedom, SS= sum of squares, MS=mean square.

Source	*DF*	**Accuracy in x-direction** (R^2=97.46%)				**Accuracy in y-direction** (R^2=89.58%)			
		Adj SS	*Adj MS*	*F-value*	*p-value*	*Adj SS*	*Adj MS*	*F-value*	*p-value*
LT	1	0.000066	0.000066	32.61	0.000	0.000055	0.000055	8.60	0.015
DE	2	0.000349	0.000175	86.24	0.000	0.000362	0.000181	28.20	0.000
PT	5	0.000123	0.000025	12.20	0.000	0.000029	0.000006	0.91	0.510
LT*DE	2	0.000165	0.000083	40.78	0.000	0.000039	0.000019	3.03	0.094
LT*PT	5	0.000011	0.000002	1.04	0.447	0.000023	0.000005	0.73	0.620
DE*PT	10	0.000062	0.000006	3.07	0.046	0.000043	0.000004	0.67	0.731
Error	10	0.000020	0.000002			0.000064	0.000006		
Total	35	0.000796				0.000616			

Table 4. ANOVA for evaluation of the influence of DE, LT, PT on x and y accuracy for PU. DF= degree of freedom, SS= sum of squares, MS=mean square.

Source	*DF*	**Accuracy in x direction** (R^2=86.80%)				**Accuracy in y direction** (R^2=94.85%)			
		Adj SS	*Adj MS*	*F-value*	*p-value*	*Adj SS*	*Adj MS*	*F-value*	*p-value*
LT	1	0.000562	0.000562	15.99	0.003	0.001237	0.001237	85.29	0.000
DE	2	0.001068	0.000534	15.20	0.001	0.000972	0.000486	33.53	0.000
PT	5	0.000041	0.000008	0.23	0.940	0.000158	0.000032	2.17	0.139
LT*DE	2	0.000066	0.000033	0.94	0.422	0.000002	0.000001	0.06	0.943
LT*PT	5	0.000208	0.000042	1.18	0.383	0.000064	0.000013	0.89	0.525
DE*PT	10	0.000365	0.000037	1.04	0.476	0.000239	0.000024	1.65	0.222
Error	10	0.000351	0.000035			0.000145	0.000015		
Total	35	0.002661				0.002817			

By analyzing the interaction effects identified as significant through ANOVA (Tables 3 and 4), it is possible to see that in the case of the accuracy in the x-direction for PB (Figure 17), the relationship between part thickness and x-direction depends on the value of DE, especially for small thicknesses. The more nonparallel the lines are, the greater the strength of the interaction. Parallel lines in an interactions plot indicate no interaction.

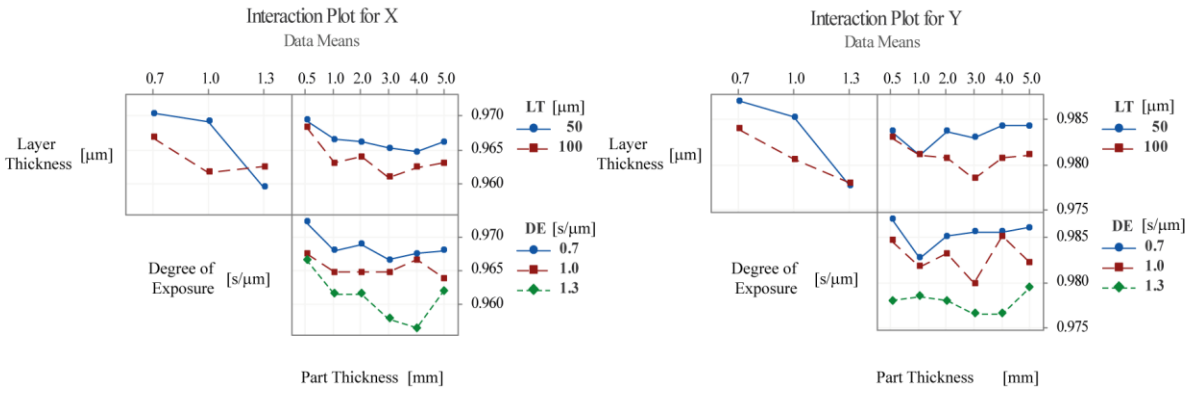

Figure 17. Interaction plot for PB.

The relationship between accuracy in x / y directions and part thickness is shown in Figure 18. The differences between the samples are very small, on the order of microns. The PB samples have a smaller deviation from the real value in the x direction only for thicknesses less than 1 mm, while it is kept more constant in the PU samples. The y direction is generally more accurate for both samples to the hundredth of a millimeter level than x and especially for PU samples less than 1 mm thick. Overall, small deviations between PU and PB in accuracy are highlighted by the results. The scattering effect should be predominant in the more loaded resin for the different optical behavior in which the ceramic particles are involved, but the results deny this prediction. Slight differences in ceramic contents found in XRD patterns can be an explanation for the dissimilarities in printing accuracy between PB and PU resins as suggested by Kovacev et al. [27]. As reported in the same study, although the energy dose should be great enough for an efficient layer curing, overgrowths in horizontal directions occur more when the energy parameters increase, following a logarithmic relation [32]. In general, the independence between solid loading and scattering phenomena can be claimed, since other aspects such as powder type, and the specific energy dose for each composition (regulated through printing parameters) further affect the printing accuracy.

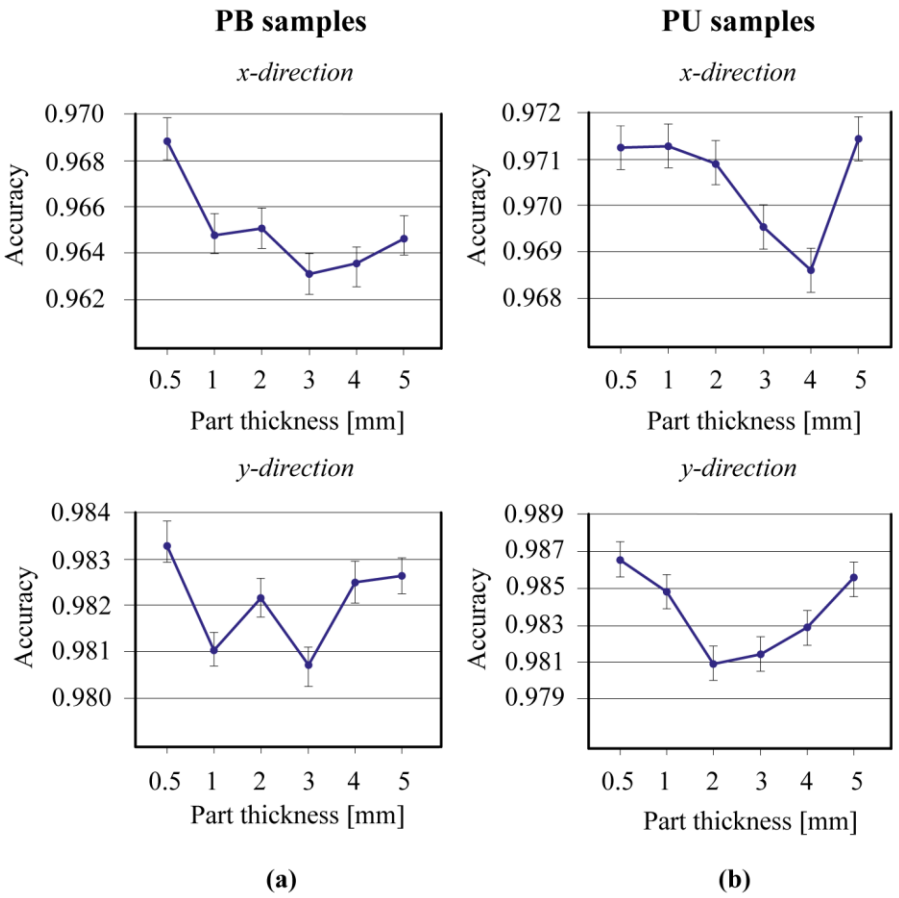

Figure 18. Relationship between accuracy in x/y directions for (a) PB samples, (b) PU samples.

3.6.2 Accuracy in z-direction

Accuracy in the z-direction, parallel to platform movement, is essentially influenced by the precision of the platform motor and by the finishing operation for supporting structures removal. The mean accuracy values for PB and PU, respectively, in the z-direction, are 94.12 ± 7.02 % and 91.36 ± 8.66%. From the ANOVA analysis (Table 5), it is possible to see that LT, part thickness, and their interaction influence the printing accuracy in the z-direction for PB, while DE and part thickness influence the accuracy for PU. The relationship between part thickness and z-direction depends on the value of LT as evidenced by the interaction plot (Figure 19).

Table 5. ANOVA for evaluation of the influence of DE, LT, PT on z accuracy for PB and PU. DF= degree of freedom, SS= sum of squares, MS=mean square.

Source	*DOF*	**PB** (R^2=97.28%)				**PU** (R^2=95.62%)			
		Adj SS	*Adj MS*	*F-value*	*p-value*	*Adj SS*	*Adj MS*	*F-value*	*p-value*
LT	1	0.050707	0.050707	108.12	0.000	0.003847	0.003847	3.34	0.097

DE	2	0.005811	0.002906	6.20	0.018	0.039358	0.019679	17.11	0.001
PT	5	0.076056	0.015211	32.43	0.000	0.169417	0.033883	29.46	0.000
LT*DE	2	0.000738	0.000369	0.79	0.482	0.002854	0.001427	1.24	0.330
LT*PT	5	0.025600	0.005120	10.92	0.001	0.006209	0.001242	1.08	0.427
DE*PT	10	0.008936	0.000894	1.91	0.162	0.029466	0.002947	2.56	0.077
Error	10	0.004690	0.000469			0.011501	0.001150		
Total	35	0.172538				0.262651			

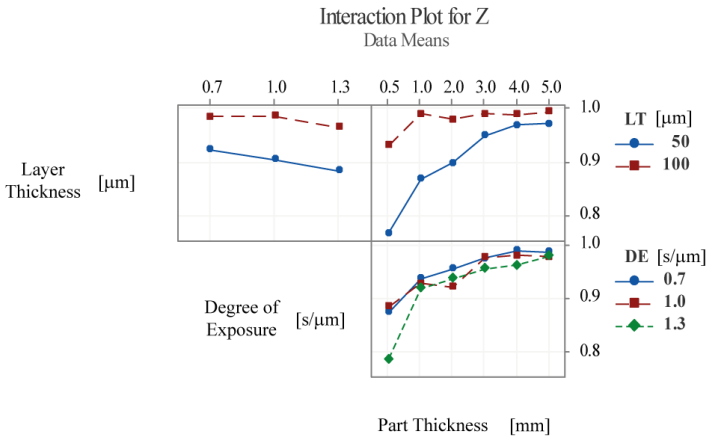

Figure 19. Interaction plot for the accuracy in the z-direction.

3.7 Volumetric shrinkage

For both resins, volumetric shrinkage was attested in a quite restricted range of variation (Figure 20). The mean values of volumetric shrinkage were 19.3 ± 2.2 % for PB resin and 41.1 ± 3.6 % for PU resin, confirming the high difference in solid loading. Data relative to PT= 0.5 mm for PU resin are unavailable due to the difficulties found when measuring the samples because of their weakness after sintering. In particular, the thinnest samples presented cracks on surfaces and heavy warping effects (Figure 14). The density of the sintered samples was relatively homogeneous, whatever the investigated printed parameters (LT and DE), and was equal to 1.25 ± 0.06 g/cm^3 and 1.73 ± 0.04 g/cm^3, respectively, for the samples prepared with the PU and the PB resin. As previously commented, these differences are due to the different solid loading values between the two resins.

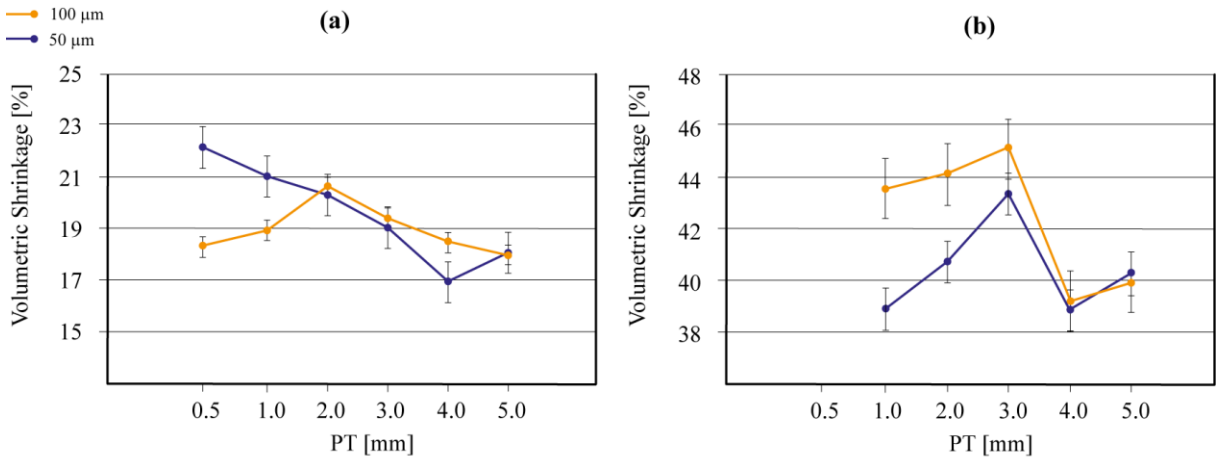

Figure 20. Volumetric shrinkage of PB (a), PU (b).

One of the implications of using a low solid loading resin in the DLP process is that if rheological stability is not verified, deposition of ceramic powder can occur during the printing process, especially for lengthy processes. Thinner samples are processed more quickly, so the percentage of ceramic content in samples can vary. Another implication in affecting the volumetric shrinkage correlated to the resin solid loading is the homogeneity of the sample; anisotropies in shrinkage are caused by the presence of a portion of samples with different percentages of the binder concerning ceramic powder, and also warping effects are favored. In this study, other process parameters have not affected the volumetric shrinkage. The same conclusion is reported in a study by Kovalenko et al. [40]. The influence on volumetric shrinkage should be due to other parameters, especially regarding the starting material, like solid loading and mean particle size and particle size distribution [39].

4. Conclusions

In the present work, different aspects regarding the complete processability of the two commercial resins have been analyzed:

- Different characterizations for the PB resin, the most loaded, were performed. Viscosity measurements revealed the relatively constant viscosity trend about the shear rate in the range from 1.42 s^{-1} to 193.6 s^{-1}, the average viscosity value was equal to 8.94 ± 0.49 Pa·s. These values are slightly higher than the ones reported in the literature for resin with comparable solid loading [3], but the processability of samples was still guaranteed. Probably, although the viscosity values exceed the target value, aspects such as the footprint of the building platform, the geometry of the samples produced, and the slow motor speed can help the processability of this resin. FESEM observation highlighted the fine granulometry of the raw powder, while XRD allowed identifying the ceramic compounds characterizing the samples. Solid loadings were evaluated through TG-DTA, and 52 wt.% for PU and 72 wt.% for PB were found.
- In the preliminary test, the problem of the cracks formed during the thermal treatment has been studied, and the window of process parameters that allow for obtaining acceptable results has been determined. TG-DTA

established a firing cycle different from the producer's recommendations, but cracks were still present in the PU resin samples. Furthermore, the cycle proposed needed a long working time, and the presence of cracks did not justify the loss in productivity.

- The process parameters considered influent in crack formation and dimensional accuracy were analyzed using a DoE approach. Cracks in PU samples were not avoided for all experimental sets tried, while in PB samples, an acceptable level of homogeneity and internal density was reached at low values of part thickness. This outcome for PB suggests that printability of bulk components with high thicknesses is not recommended, but a good result can be reached for lattice or emptied components.
- Accuracy values reached in x and y directions are respectively 96.50 ± 0.48 % and 98.21 ± 0.42 % for PB, 97.05 ± 0.87 % and 98.37 ± 0.9 % for PU. Statistical analyses highlight that LT and DE influence accuracy in both directions and for both resins, part thickness influences accuracy only in the x-direction for PB resin, especially for the thinnest samples. In the z-direction, the accuracy of 94.12 ± 7.02 % and 91.36 ± 8.66%, respectively, for PU and PB were achieved. LT, PT, and their interaction are influential in the z-direction. The printed accuracy shows certain independence from the resin solid loading.
- Volumetric shrinkage found for PB, and PU were 19.3 ± 2.2 % and 41.1 ± 3.6 %, respectively. For PU sintered samples with small part thickness, measurements are not available because of the high warping. As expected, the higher solid loading of the PB resin led to a much lower shrinkage during the thermal treatment and limited the cracks and deformations in the fired samples.

Knowledge of the exact composition of the resin used in stereolithographic applications allows for predicting the optimal process and post-process conditions and obtaining dense objects with dimensional and mechanical properties adequate for the desired applications. This study highlights that the processability of commercial resins with unknown composition and solid loading leads to difficulties in several aspects, so a deep investigation needs to be performed to understand the specific process.

Acknowledgments

The Authors greatly thank the SISCON Interdepartmental Center (Safety of Infrastructures and Constructions) for the use of instruments (rheometer and TG-DTA).

CRediT authorship contribution statement

Alessandro Bove: Methodology, Formal analysis, Investigation, Validation, Writing - original draft preparation, Writing - review and editing. Jean-Marc Tulliani: Methodology, Formal analysis, Investigation, Validation, Writing - original draft preparation, Writing - review and editing. Manuela Galati: Conceptualization, Writing - review and editing. Flaviana Calignano: Supervision, Resources, Conceptualization, Methodology, Formal analysis, Writing - original draft preparation, Writing - review and editing

Competing Interests

The authors have no relevant financial or non-financial interests to disclose.

References

1. Trombetta R, Inzana JA, Schwarz EM, et al (2017) 3D Printing of Calcium Phosphate Ceramics for Bone Tissue Engineering and Drug Delivery. Ann Biomed Eng 45:23–44. https://doi.org/10.1007/s10439-016-1678-3

2. da Silva LRR, Sales WF, Campos F dos AR, et al (2021) A comprehensive review on additive manufacturing of medical devices. Prog Addit Manuf 6:517–553. https://doi.org/10.1007/S40964-021-00188-0

3. Hinczewski C, Corbel " S, Chartier T (1998) Ceramic Suspensions Suitable for Stereolithogiaphy. J Eur Ceram Soc 18:583–590

4. Santoliquido O, Colombo P, Ortona A (2019) Additive Manufacturing of ceramic components by Digital Light Processing: A comparison between the “bottom-up” and the “top-down” approaches. J Eur Ceram Soc 39:2140–2148. https://doi.org/10.1016/j.jeurceramsoc.2019.01.044

5. Nötzel D, Eickhoff R, Hanemann T (2018) Fused filament fabrication of small ceramic components. Materials (Basel) 11:. https://doi.org/10.3390/ma11081463

6. Lv X, Ye F, Cheng L, et al (2019) Binder jetting of ceramics: Powders, binders, printing parameters, equipment, and post-treatment. Ceram. Int. 45:12609–12624

7. Shakor P, Chu · S H, Puzatova A, Dini E (2008) Review of binder jetting 3D printing in the construction industry. Prog Addit Manuf. https://doi.org/10.1007/s40964-021-00252-9

8. Sing SL, Yeong WY, Wiria FE, et al (2017) Direct selective laser sintering and melting of ceramics: A review. Rapid Prototyp. J. 23:611–623

9. Chen Z, Li Z, Li J, et al (2019) 3D printing of ceramics: A review. J. Eur. Ceram. Soc. 39:661–687

10. An D, Li H, Xie Z, et al (2017) Additive manufacturing and characterization of complex Al2O3 parts based on a novel stereolithography method. Int J Appl Ceram Technol 14:836–844. https://doi.org/10.1111/ijac.12721

11. de Hazan Y, Penner D (2017) SiC and SiOC ceramic articles produced by stereolithography of acrylate modified polycarbosilane systems. J Eur Ceram Soc. https://doi.org/10.1016/j.jeurceramsoc.2017.03.021

12. Lee YH, Lee J Bin, Maeng WY, et al (2019) Photocurable ceramic slurry using solid camphor as novel diluent for conventional digital light processing (DLP) process. J Eur Ceram Soc. https://doi.org/10.1016/j.jeurceramsoc.2019.05.069

13. Minas C, Carnelli D, Tervoort E, Studart AR (2016) 3D Printing of Emulsions and Foams into Hierarchical Porous Ceramics. Adv Mater. https://doi.org/10.1002/adma.201603390

14. Shao H, Zhao D, Lin T, et al (2017) 3D gel-printing of zirconia ceramic parts. Ceram Int.

https://doi.org/10.1016/j.ceramint.2017.07.124

15. Chen Z, Sun X, Shang Y, et al (2021) Dense ceramics with complex shape fabricated by 3D printing: A review. J. Adv. Ceram.

16. Bove A, Calignano F, Galati M, Iuliano L (2022) Photopolymerization of Ceramic Resins by Stereolithography Process: A Review. Appl Sci 12:. https://doi.org/10.3390/app12073591

17. Bae CJ, Halloran JW (2011) Integrally cored ceramic mold fabricated by ceramic stereolithography. Int J Appl Ceram Technol. https://doi.org/10.1111/j.1744-7402.2010.02568.x

18. Johansson E, Lidström O, Johansson J, et al (2017) Influence of resin composition on the defect formation in alumina manufactured by stereolithography. Materials (Basel) 10:. https://doi.org/10.3390/ma10020138

19. Li S, Duan W, Zhao T, et al (2018) The fabrication of SiBCN ceramic components from preceramic polymers by digital light processing (DLP) 3D printing technology. J Eur Ceram Soc. https://doi.org/10.1016/j.jeurceramsoc.2018.06.046

20. Tomeckova V, Halloran JW (2010) Critical energy for photopolymerization of ceramic suspensions in acrylate monomers. J Eur Ceram Soc. https://doi.org/10.1016/j.jeurceramsoc.2010.08.003

21. Goswami A, Ankit K, Balashanmugam N, et al (2014) Optimization of rheological properties of photopolymerizable alumina suspensions for ceramic microstereolithography. Ceram Int 40:3655–3665. https://doi.org/10.1016/j.ceramint.2013.09.059

22. Truxova V, Safka J, Seidl M, et al (2020) Ceramic 3d printing: Comparison of SLA and DLP technologies. MM Sci J 2020:3905–3911. https://doi.org/10.17973/MMSJ.2020_06_2020006

23. Mei H, Zhao R, Xia Y, et al (2019) Ultrahigh strength printed ceramic lattices. J Alloys Compd 797:786–796. https://doi.org/10.1016/J.JALLCOM.2019.05.117

24. Mummareddy B, Maravola M, MacDonald E, et al (2020) The fracture properties of metal-ceramic composites manufactured via stereolithography. Int J Appl Ceram Technol 17:413–423. https://doi.org/10.1111/ijac.13432

25. Schwentenwein M, Homa J (2015) Additive manufacturing of dense alumina ceramics. Int J Appl Ceram Technol 12:1–7. https://doi.org/10.1111/ijac.12319

26. Car F, Brnadić G, Tomašić V, Domagoj Vrsaljko · Advanced preparation method of monolithic catalyst carriers using 3D-printing technology. Prog Addit Manuf. https://doi.org/10.1007/s40964-022-00266-x

27. Kovacev N, Li S, Essa K (2021) Effect of the preparation techniques of photopolymerizable ceramic slurry and printing parameters on the accuracy of 3D printed lattice structures. J Eur Ceram Soc 41:7734–7743. https://doi.org/10.1016/j.jeurceramsoc.2021.08.052

28. Wang X, Zou B, Li L, et al (2021) Manufacturing of a ceramic groove part based on additive and subtractive technologies. Ceram Int 47:740–747. https://doi.org/10.1016/j.ceramint.2020.08.184

29. Yadegari F, Fesharakifard R, Barazandeh F Numerical and experimental investigation of effective parameters on separation force in bottom-up stereolithography process

30. Zakeri S, Vippola M, Levänen E (2020) A comprehensive review of the photopolymerization of ceramic resins used in stereolithography. Addit. Manuf. 35

31. Llanos Peñaloza GA (2018) Additive Manufacturing of Zirconia. Chalmers University of Technology

32. Gentry SP, Halloran JW (2013) Depth and width of cured lines in photopolymerizable ceramic suspensions. J Eur Ceram Soc 33:1981–1988. https://doi.org/10.1016/J.JEURCERAMSOC.2013.02.033

33. Li X, Zhang H, Shen Y, et al (2021) Fabrication of porous β-TCP/58S bioglass scaffolds via top-down DLP printing with high solid loading ceramic-resin slurry. Mater Chem Phys 267:. https://doi.org/10.1016/j.matchemphys.2021.124587

34. Malvern Instruments (2012) Understanding Yield Stress. Annu Trans Nord Rheol Soc 21:6

35. Chen YF, Wang MC, Hon MH (2003) Pore Structure and Permeation Properties of Kaolin-Silica-Alumina Ceramics. J Ceram Soc Japan 111:537–543. https://doi.org/10.2109/jcersj.111.537

36. G. Fantozzi, J.C. Nièpce GB (2013) Les Céramiques réfractaires. In: Dunod (ed) Les Céramiques industrielles. Paris, France, pp 119–156

37. Wang K, Qiu M, Jiao C, et al (2020) Study on defect-free debinding green body of ceramic formed by DLP technology. Ceram Int 46:2438–2446. https://doi.org/10.1016/j.ceramint.2019.09.237

38. Johansson E, Lidström O, Johansson J, et al (2017) materials Influence of Resin Composition on the Defect Formation in Alumina Manufactured by Stereolithography. https://doi.org/10.3390/ma10020138

39. Chen Z, Liu C, Li J, et al (2019) Mechanical properties and microstructures of 3D printed bulk cordierite parts. Ceram Int 45:19257–19267. https://doi.org/10.1016/j.ceramint.2019.06.174

40. Kovalenko I, Ramachandran Y, Garan M (2019) Experimental shrinkage study of ceramic DLP 3D printed parts after firing green bodies in a KILN. MM Sci J 2019:2767–2771. https://doi.org/10.17973/MMSJ.2019_03_2018113